Non-invasive estimation of moisture content in tuff bricks by GPR

Agliata, Rosa; Bogaard, Thom A.; Greco, Roberto; Mollo, Luigi; Slob, Evert C.; Steele-Dunne, Susan C.

DOI
10.1016/j.conbuildmat.2017.11.103

Publication date
2018

Document Version
Accepted author manuscript

Published in
Construction and Building Materials

Citation (APA)
Agliata, R., Bogaard, T. A., Greco, R., Mollo, L., Slob, E. C., & Steele-Dunne, S. C. (2018). Non-invasive estimation of moisture content in tuff bricks by GPR. *Construction and Building Materials*, *160*, 698-706. https://doi.org/10.1016/j.conbuildmat.2017.11.103

Non-invasive estimation of moisture content in tuff bricks by GPR

Rosa Agliata[a*], Thom A. Bogaard[b], Roberto Greco[a], Luigi Mollo[a], Evert C. Slob[c], Susan C. Steele-Dunne[b]

[a] *Università della Campania "L. Vanvitelli", Dpt di Ingegneria Civile Design Edilizia e Ambiente, via Roma 9, 81031, Aversa (CE), Italy*
[b] *Delft University of Technology, Dpt of Water Management, PO-box 5048, 2600GA Delft, The Netherlands*
[c] *Delft University of Technology, Dpt of Geoscience and Engineering, PO-box 5048, 2600GA Delft, The Netherlands*
** corresponding author, email: rosa.agliata@unicampania.it*

Abstract

Measuring water content in buildings of historical value requires non-invasive techniques to avoid the damage that sample taking or probe insertion may cause to the investigated walls. With this aim, a stepped frequency ground penetrating radar (GPR) system was tested to assess its applicability in moisture measurements of porous masonry elements. The technique was tested on a real scale wall made with yellow Neapolitan tuff bricks, a material commonly found in historical buildings of Campania (Southern Italy). First, the antenna was calibrated to find its characteristic transfer functions. Then 64 GPR acquisitions, coupled with gravimetric measurements of the volumetric water content, were performed on the tuff wall in laboratory controlled conditions. A full inverse modelling of the GPR signal on tuff was used to retrieve dielectric permittivity and electrical conductivity of tuff at various water contents. By linking these characteristic electromagnetic parameters to the water content, the calibration relationships specific for yellow Neapolitan tuff are defined, which can be used for moisture measurements by GPR in real case studies. The experimental results lead to a robust identification of clearly defined monotonic relationships for dielectric permittivity and electrical conductivity. These are characterized by high values of the correlation coefficient, indicating that both parameters are potentially good proxies for water content of tuff. The results indicate that GPR represents a promising indirect technique for reliable measurements of water content in tuff walls and, potentially, in other porous building materials.

Keywords: moisture, non-invasive measurement, tuff masonry, ground penetrating radar, inverse modelling

1. Introduction

Measuring the water content of building materials is essential to prevent the damage that moisture may cause to construction elements such as walls, but also to the plaster that protects them and even to frescoes covering it. The moisture content and its distribution in a building should be repeatedly evaluated in the easiest and least-invasive way possible. Based on such monitoring results, more effective decisions for renovation or restoration can be made.

Volcanic tuff is among the building materials that show the highest ability to absorb and retain water [1,2]. It is a natural pyroclastic stone, which is widespread in Campania (Southern Italy), where it has been used for centuries to build vertical barriers of any kind of construction, including heritage buildings. Common destructive or invasive methods cannot be used in buildings of historical value for measuring moisture content, because the walls of those structures are often covered by frescos or valuable plasters. Hence, novel approaches are needed to estimate the water content in porous building materials in a non-invasive way. Over the years, many different techniques have been tested, such as gamma ray attenuation [3,4], infrared thermography [5,6], neutron radiography [7], capacitance methods [8], non-invasive time domain reflectometry [9,10,11], x-ray radiography [12,13], impedance tomography [14], evanescent-field dielectrometry [15], high-frequency sensors [16], wireless inductive-capacitive sensors [17], and, recently, early stage optic fibre sensors prototypes [18]. The dependence of bulk relative dielectric permittivity (ε_r) and bulk electrical conductivity (σ) of porous media on their water content is indeed well known [19] and most of the above mentioned techniques rely on that.

Another experimental technique sensitive to electric properties of materials and used to map the shallow subsurface with high resolution is ground penetrating radar (GPR). It operates through electromagnetic radiation in the microwave band of the radio spectrum, with frequencies typically comprised between a few MHz and 5 GHz [20]. The transmitting antenna of the GPR system generates a signal, which propagates through the material with a speed related to the dielectric permittivity of the medium, assuming the magnetic permeability is that of free space. The reflected signal from the subsurface is detected by the receiving antenna [21]. Thanks to its safe, rapid, non-destructive and non-invasive features, GPR continues to find more civil engineering applications [22]. GPR is an established method to assess the presence of cracks in road and highway pavements [23], bridges [24] and tunnels, and to perform in-situ quality control of density and moisture content of fresh bituminous mixtures [25,26]. In addition, the GPR method is widely used in geological surveys to detect subsurface cavities and voids [27], map soil layers and texture [28], and to image the foundations of buildings and their surroundings [29]. Another successful application of GPR is the discovery of buried archaeological objects [30] and underground utilities such as gas and water pipes [31]. GPR can also be used to evaluate the electromagnetic properties [32,33] and moisture content of soils [34,35,36].

In the building industry, subsurface remote sensing is a useful tool to detect inclusions [21], voids [37,38] and damage [39,40,41] and to measure the water content [42,43,44,45,46,47,48] over a wide area of a construction in a non-invasive way. It is worth noting that this analysis enables to obtain a more complete picture of the state of health of a building than single-point tests (e.g. drilling) [49].

In this study the feasibility of using the GPR technique to measure the moisture content in yellow volcanic tuff masonry without damaging the historical heritage is evaluated. The procedure to characterize the response of the antenna and the forward model adopted for GPR data processing are described. Then, the results of GPR experiments on a real scale wall are presented, with the aim of calibrating the GPR response to water content variations. The relationships linking dielectric permittivity and electrical conductivity of volcanic tuff to its volumetric water content are identified. Finally, the quality with which the water content can be estimated from GPR reflection data is assessed. This initial calibration phase is indeed essential to carry out GPR surveys in real case studies.

2. Theory of ground-penetrating radar system

A stepped frequency continuous wave (SFCW) radar, combined with a dielectric-filled transverse electric and magnetic (TEM) linear polarized double ridged broadband horn antenna (BBHA 9120 A, Schwarzbeck - Mess-Elektronik) used off-ground in monostatic mode (i.e. a single antenna used as emitter and receiver) was used to map the dielectric permittivity and electrical conductivity of the subsurface. This radar configuration allows an effective and realistic modelling of the radar-antenna-subsurface system [50]. A SFCW radar enables the user to control an ultra-wide frequency band (UWB) that results in a finer depth resolution. Moreover, for this type of radar, the effect of the dispersive properties of the UWB antennas on the measurements can be taken into account by performing a prior calibration. Performing measurements with an SFCW radar has two more advantages over those with a pulse radar. Firstly, pulse radars are subsampled and require many emissions to build a measurement in the time window of interest, whereas at each frequency an independent measurement is taken. Secondly, at each frequency the same signal strength can be achieved, whereas for pulse radars most of the energy is concentrated around a so-called centre frequency. A ZVH8 Cable and Antenna Analyzer (ZVH8, 100 kHz to 8Ghz, Rohde & Schwarz, München, Germany) with the K42 Vector Network Analyzer and K40 Remote Control options was used to emulate an UWB-SFCW radar system. The antenna is 195 mm long, has an aperture of 245 x 142 mm^2, and operates in the range of 0.8 – 5 GHz. It was connected to Port 1 of the VNA via an N-type 50 Ohm coaxial cable. This setup allows for a measured GPR signal consisting of the complex ratio $S_{11}(\omega)$ between the reflected signal and the emitted signal, ω being the angular frequency [51].

The VNA was calibrated at the connection between its feed point and the cable using the *Open, Short* and *Match* loads of a high precision standard calibration kit (85032B Type-N, 50 Ohm, Keysight Technologies). This procedure is necessary to establish a reference plane where S_{11} is measured. The radar-antenna-subsurface system was modelled using the block diagram shown in Fig.1, as introduced by Lambot et al. [32]. The proposed model for describing the radar signal is based on two main assumptions. First, the shape of the electromagnetic field received by the antenna is independent of the target, meaning that only the phase and amplitude of the field are functions of the target. This assumption has been proven to be valid when the investigated surface is situated in the far-field region of the antenna [32,33], which can then be modelled accurately as an interactive point source and point receiver rather than as a spatially distributed source and receiver. Second, the subsurface can be described as a horizontally layered medium [51], which is a consequence of the first assumption, provided that any horizontal variability of the electric properties of the investigated medium is neglected.

The measured signal can be given in terms of the earth's impulse reflection response and the antenna transfer functions, expressed in the frequency domain as

$$S_{11}(\omega) = \frac{b(\omega)}{a(\omega)} = H_i(\omega) + \frac{H(\omega)G_{xx}(\omega)}{1-H_f(\omega)G_{xx}(\omega)} \quad (1)$$

where $b(\omega)$ and $a(\omega)$ are received and emitted signals at the VNA reference plane, respectively. $H_i(\omega)$ is the return loss, $H(\omega) = H_t(\omega)H_r(\omega)$ is the transmitting-receiving transfer function, $H_f(\omega)$ is the feedback loss, and $G_{xx}(\omega)$ is the earth's impulse reflection response, also known as the scattered Green's function [52,53,54] of the air-subsurface system, modelled as a layered medium. For this model configuration, the approach given in Slob and Fokkema [55] and Lambot et al. [51] is used to determine $\mathbf{G_{xx}(\omega)}$ (that is the the exact solution of the 3-D Maxwell's equations for wave propagation in a horizontally multilayered medium) by computing recursively the transverse electric and magnetic global reflection coefficients of the multilayered system in the two-dimensional spatial Fourier domain.

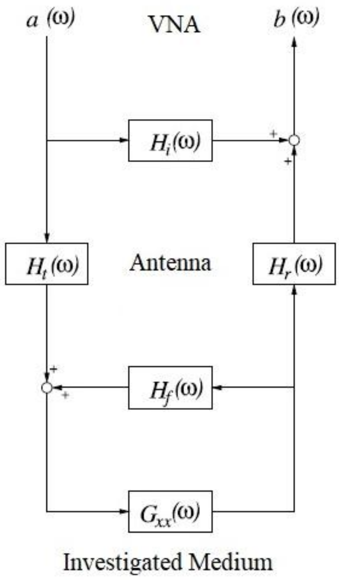

Fig. 1 Block diagram representing the radar-antenna-subsurface system, modelled as linear systems in series and parallel, where *a(ω)* and *b(ω)* are the emitted and received waves at the VNA reference plane, respectively; $H_i(\omega)$ is the return loss; $H_t(\omega)$ and $H_r(\omega)$ are the transmitting and receiving transfer functions, respectively; $H_f(\omega)$ is the feedback loss; and $G_{xx}(\omega)$ is the transfer Green's function of the air-subsurface system (redrawn after [50]).

2.1 Calibration of the antenna

In the adopted setup, a metal plate was placed centrally below the antenna, as shown in Fig. 2a. It is large enough to be modelled as an infinite perfect electric conductor. The antenna transfer functions $H_i(\omega)$, $H(\omega)$ and $H_f(\omega)$, can be obtained by solving equation (1) for different distances between the metal plate and the antenna aperture. More than 3 different configurations should be used to overcome possible problems with numerical instability of the solution at some frequencies [50]. Here 11 different distances were used, ranging between 25 cm and 35 cm (25, 25.8, 26.6, 27.6, 28.6, 29.7, 30.6, 31.6, 32.5, 33.6 and 34.8 cm). The anticipated experiments should be taken somewhere inside this range and the range is the interval where the assumptions are deemed valid.

For each height, the $S_{11}(\omega)$ functions can be measured and the Green's functions $G_{xx}(\omega)$ can be computed. The unknown transfer functions are then found from the measured $S_{11}$by minimizing equation (1) in the least squares sense using all distances.

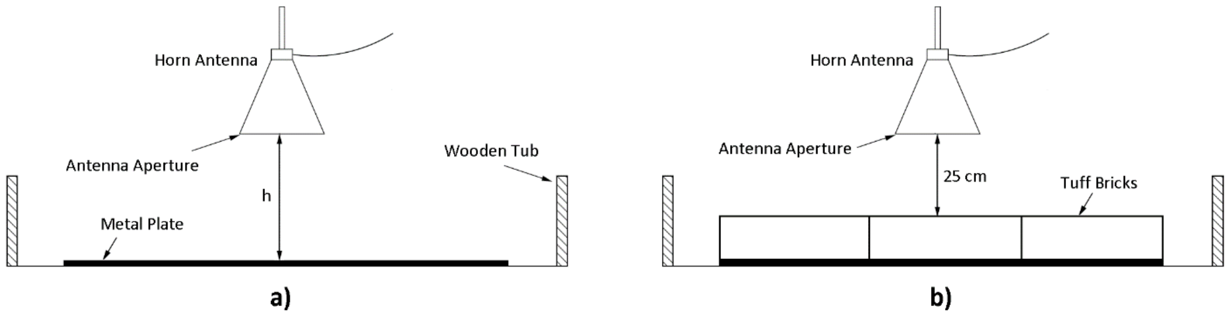

Fig. 2 Sketches of the experimental setup adopted for the calibration of the antenna (a) and for the determination of the relationships linking dielectric permittivity and electrical conductivity of tuff with its volumetric water content (b).

2.2 Tuff bricks electric properties

The constitutive parameters governing electromagnetic wave propagation are dielectric permittivity ε (Fm^{-1}), electrical conductivity **σ** (Sm^{-1}), and magnetic permeability μ (Hm^{-1}). The latter can be assumed equal to the permeability of free space ($\mu_0 = 4\pi \times 10^{-7}$ Hm^{-1}), which is valid for non-magnetic materials, as in the present case. The relative dielectric permittivity is defined as $\varepsilon_r = \varepsilon/\varepsilon_0$, where $\varepsilon_0 = 1/(\mu_0 c_0^2)$ is the permittivity of free space ($c_0 = 2.998 \times 10^8 ms^{-1}$ being the speed of electromagnetic waves in vacuum).

The relative dielectric permittivity is considered independent of the frequency while the electrical conductivity can depend on frequency as a consequence of relaxation mechanisms as well as the Maxwell-Wagner effect [56,57,58,59,33]. To determine if σ is frequency dependent, it was first considered independent and then linearly dependent on frequency as described by:

$$\sigma(f) = \sigma_{1GHz} + a\,(f - 10^9) \qquad (2)$$

where f is the frequency, σ_{1GHz} is the reference electrical conductivity at 1 GHz, and a is the slope of σ(f). The electrical conductivity of sandy soils can be well estimated by equation (2) when the frequency ranges from 1 to 3 GHz. For this reason 3 GHz is taken as the upper limit (f_{max}) of the experiment, as the electrical conductivity of tuff is assumed to be similar to that of sand (0.01 – 1 Sm^{-1}). 0.8 GHz was chosen as the lower limit (f_{min}), which is the minimum operational frequency of the antenna. The attenuation of the wave amplitude along the two-way travel path through the tuff bricks (i.e. 21 cm) was such that the reflected signal was clearly detectable across the entire range of frequency, thus allowing a reliable estimate of the electric properties of the investigated medium. In fact, the worst condition occurs at f_{max} near saturation conditions, when the high values of electrical conductivity and permittivity cause the biggest attenuation. Being the skin depth (s_d) the distance at which the wave amplitude decreases to $1/e^2$ of the emitted value, this distance can be calculated by [60]:

$$s_d = \frac{\mathrm{c}}{2\pi f\sqrt{\frac{\varepsilon_r}{2}\left[\sqrt{1+\left(\frac{\frac{\sigma}{2\pi f\varepsilon_0}}{\varepsilon_r}\right)^2}-1\right]}} \tag{3}$$

In the worst condition, brick thickness is about 1.36^*s_d , indicating full penetration of the signal.

In the considered interval, S_{11} was acquired sequentially at 1201 stepped operating frequencies with a frequency step of around 1.8 MHz.

2.3 Modelling of the Radar Signal: Model Inversion

Subsurface parameter identification was formulated as an inverse problem in the least squares sense and an objective function to be minimized, expressing the amplitude of the model errors as a Normalized Root Mean Square Error (NRMSE), was defined as follows [40]:

$$\varphi(\mathrm{b}) = \left(\frac{\sum_{\mathrm{fmin}}^{\mathrm{fmax}}\left|\mathrm{G}_{\mathrm{xx}}^{\mathrm{obs}} - \mathrm{G}_{\mathrm{xx}}^{\mathrm{pre}}\right|^2}{\sum_{\mathrm{fmin}}^{\mathrm{fmax}}\left|\mathrm{G}_{\mathrm{xx}}^{\mathrm{obs}}\right|^2}\right)^{1/2} \tag{4}$$

where $\mathbf{G}_{\mathbf{xx}}^{\mathbf{obs}} = \mathrm{G}_{xx}^{obs}(\omega)$ and $\mathbf{G}_{\mathbf{xx}}^{\mathbf{pre}} = \mathrm{G}_{xx}^{pre}(\omega, \mathbf{b})$ are the complex vectors containing the observed and the predicted Green's functions, respectively. The parameter vector $\mathbf{b}$ contains the unknowns and is given by $\mathbf{b} = [\varepsilon_r, \sigma]$ (or $\mathbf{b} = [\varepsilon_r, \sigma_{1\mathrm{GHz}}, a]$ when σ is considered as frequency dependent).

To find estimates for the unknowns, the objective function $\varphi(\mathbf{b})$ should be minimized. This minimization problem is ill-posed and non-unique, and the objective function may present many local minima. Usually, this problem is solved by iterative forward modelling with the aim to minimize the number of iterations necessary to find the best estimate for the unknown parameters. In this case, given the limited number of parameters to be identified, a full solution space can be explored with a metaheuristic variable neighbourhood search method [61]. A large parameter space ($1<\varepsilon_r<20$; $1\text{x}10^{-3}<\sigma_{1GHz}<1\text{x}10^{-1}$ Sm^{-1}; $1\text{x}10^{-12}<\alpha<1\text{x}10^{-10}$ Ssm^{-1}) was investigated to avoid local minima of the objective function. This is initially done with relatively large steps, such that subsequent investigations are performed in a smaller region of the parameter space around the provisional local minimum until the best estimate is found, representing the solution of the inverse problem.

3. Materials and methods

3.1 Experimental Setup and procedure

For the test, 15 bricks of yellow volcanic tuff (porosity = 50% [2,62]) were acquired from a surface quarry in Quarto, near Naples, southern Italy. The average dimensions of each tuff brick are 10 x 24 x 38 cm (average volume 9.2 dm^3). The dry bulk density of the bricks (γ) was calculated by measuring the mass and volume of 6 of the bricks and averaging the obtained values. The soaking ratio was experimentally determined as the ratio between the mass of water absorbed at saturation by one brick and its oven-dried mass.

The bricks were arranged in the form of a horizontal wall, with one of the two major surfaces lying on the ground (Fig. 2b). This arrangement prevented the formation of horizontal moisture gradients within the experimentally investigated area, as required by the second assumption stated in section 2.1. To avoid distortions due to air gaps, quick-setting cement was used to assemble the stones together to fill the fissures at the interface of bricks (see subsection 2.2.1).

The assembled wall, measuring approximately 123 x 110 cm, was built in a tub with wooden frames (inner dimensions 190 x 160 cm), in an indoor environment under controlled temperature (18-20° C) and relative humidity (RH≈0.7). The tub was made impervious by covering the inner surface with a double layer of strong plastic sheet. Below the plastic sheet, a horizontal metal plate was installed to control the bottom boundary conditions in the electromagnetic model, so that materials placed underneath the metal plate had no influence on the measured backscattered signal. The antenna was located 25 cm above the surface of the tuff bricks, with a footprint (at this height and for the considered frequency interval) of around 80 x 80 cm.

Ten microwave absorbing foam panels, with the dimensions of 70 x 70 cm, were placed around the tub to prevent the measurements being influenced by the presence of metal objects around the setup that could cause spurious reflections in the backscattered signal.

A prism-shaped sample (14 x 24 x 9.5 cm), used as a reference, was obtained by cutting off one half from one of the 15 bricks, and coated on the side surfaces with waterproofing spray to mimic the moisture conditions of the bricks located in the middle of the wall. The sample stone was placed in the tub beside the tested wall and served as gravimetric reference to retrieve the amount of water contained in the bricks, by weighing it using an electronic balance (FKB by KERN & SOHN GmbH) with an accuracy of 0.1 g.

The experimental setup is shown in Fig. 3. Before wetting the wall, a GPR response was acquired and the weight of the sample stone measured. Then, the wall and the sample stone were submerged for 42 hours. When saturation was achieved, water was removed from the tub with a pump, and the drying phase started. During this phase, the sample stone was weighed at different time intervals for 15 days. Simultaneously, the GPR waveforms were acquired every 5 minutes in the beginning of the experiment, and increasing up to 15 minutes when reaching the end of the experiment. A total of 64 coupled acquisitions were made.

When the experiment ended, the sample was subjected to a drying stage in a stove at 105°C for 48 h. The weight of the oven-dried sample stone was used as a reference to calculate the volumetric water content of the sample stone at each gravimetric measurement [63].

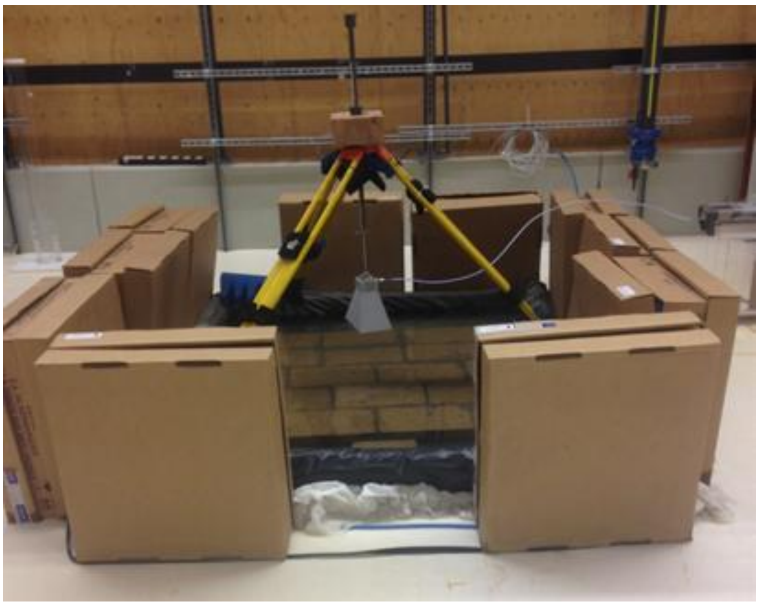

Fig. 3 View of the experimental setup

3.2 Surface Roughness Characterization

Surface roughness can be considered as a major source of noise in subsurface mapping [64]. If the top surface is smooth, then the back reflected signal would be mostly consisting of specular reflection, meaning that the incident and the reflected rays would have the same angle of incidence. On the other hand, if the surface is rough, then diffuse reflection might occur. Indeed, the incident ray reaching the surface of the medium, would be split and reflected back at many angles rather than one, by localized irregularities of the surface, causing distortion of electromagnetic signals. This effect, also known as scattering, needs to be taken into account in signal processing (e.g. [65,50]).

The most commonly used criterion to define a surface as smooth or rough, from an electromagnetic point of view, is Rayleigh's criterion (e.g. Boithias [66]). For a monostatic mode of operation (adopted in this study), a surface is considered rough if the average height of the surface protrusions is bigger than the critical height ($h_m \geq h_c$). The critical height could be described as function of the wavelength (λ)

$$h_c = \lambda/8 \quad (5)$$

with $\lambda = c_0/f$.

Alternatively, the surface roughness of the tuff bricks was measured by a Terrestrial Laser Scanning (TLS) survey, using a Leica C10 laser scanner, with the tuff bricks juxtaposed next to each other, over an area of 75 x 75 cm^2, contained in the antenna footprint.

4. Results and Discussion

4.1 Characterization of the bricks

The calculated dry bulk density and the soaking ratio of the bricks were 1.33 kg/dm^3 and 24%, respectively. These values are consistent with the typical literature values for yellow Neapolitan tuff [2,53].

Regarding the surface roughness characterization, the critical height (h_c) of the protuberances calculated, according to equation (5), for the lowest (0.8 GHz) and the highest (3 GHz) used frequencies were 4.70 cm and 1.25 cm, respectively. The results of the laser scan test, shown in Fig. 4, highlighted that the maximum height of the surface protuberances (h_{max}) was smaller than 0.6 cm, which is perfectly compatible with the GPR requirements ($h_{max}<h_c$). Conversely, the dimension of the fissures between the bricks (reaching 1.5 cm)

exceeded the critical height at high frequencies, so it could affect the measurements. For this reason, the gaps were all sealed with a cement admixture before starting the acquisitions with GPR, as explained in section 2.2.

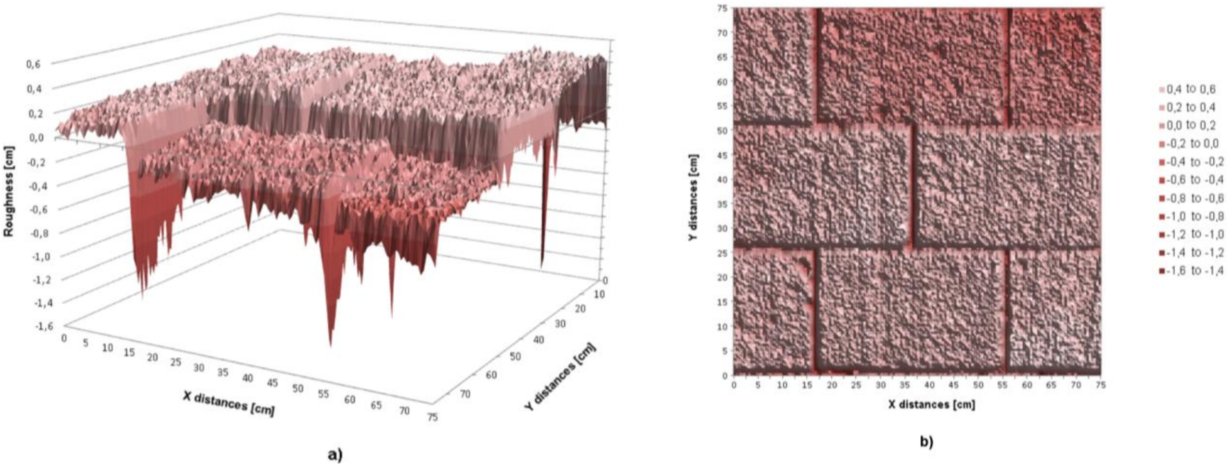

Fig. 4 Characterization of the surface roughness recorded by the laser scanner in 3D view (a) and intensity colour map (b)

4.2 Characterization of the Antenna

As explained in section 2.1.1, the characterization of the antenna consists of a series of measurements to determine the antenna transfer functions.

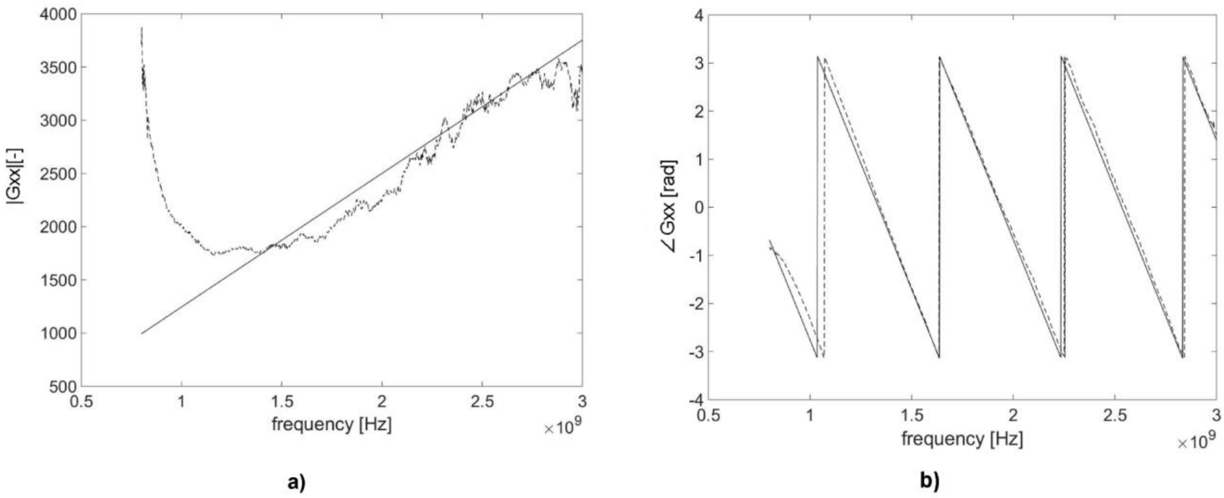

Fig. 5 Observed (dashed line) and predicted (solid line) Green's function in air (antenna characterization phase) at 25 cm distance from the metal plate: amplitude vs. frequency (a); phase angle vs. frequency (b)

As an example, Fig. 5 shows the observed and predicted Green's response functions during the characterization of the antenna, when the latter was suspended at 25 cm distance from the metal plate. This fixed distance was also adopted during the entire experiment on tuff. It can be observed from Fig. 5 that the phase (Fig. 5b) is better reproduced than the amplitude (Fig. 5a). The predicted Green's function amplitudes show a global NRMSE of 0.252. However, considering only the range 1.2 – 3 GHz, the calculated NRMSE decreases to 0.158. The agreement between observed and predicted phase shown in Fig. 5b is satisfactory over the entire investigated frequency interval. In view of the error values, the experimental results are analysed only within the 1.2 – 3 GHz frequency range.

4.3 Characterization of GPR response of tuff

As indicated in section 2.1.2, for the modelling of the Green's functions simulating the response of GPR on tuff, two alternative assumptions were made: a) no dependence of the electrical conductivity on frequency; b) electrical conductivity linearly dependent on frequency, according to equation (2). The results obtained indicate that, for the considered frequency interval, the use of equation (2) does not lead to a significant improvement of the ability of the model to reproduce the observed Green's function. The objective function ϕ, ranging between 0.346 and 0.536 in both cases, reveals a slight improvement only in few cases, with the maximum improvement of 0.04 achieved in the driest tested conditions. Furthermore, the introduction of an additional parameter to be identified with the inverse modelling (namely, the two parameters σ_{1GHz} and a of equation (2) in place of the constant σ), results in a more complex inverse problem and did not improve the identification of the searched characteristic relationships $\theta(\varepsilon_r)$ and $\theta(\sigma)$ holding for tuff. Concerning the inversely estimated relationship $\theta(\varepsilon_r)$, there is almost no difference whether the electrical conductivity is considered dependent on frequency or not. Therefore, the identified ε_r values are nearly the same and the two curves, describing the best-fitting calibration relationships $\theta(\varepsilon_r)$, perfectly overlay. Conversely, when the electrical conductivity is considered dependent on frequency, it is no longer possible to establish a $\theta(\sigma)$ relationship, unless we consider the value of σ at 1GHz. The obtained (θ, σ_{1GHz}) points, however, do not show a physically sound monotonic pattern, leading to an ill-defined $\theta(\sigma_{1GHz})$ relationship. For all these reasons, the results presented hereafter assume that σ is independent of frequency.

The minimum values of the objective function φ of equation (4), obtained for the 64 coupled acquisitions, indicate that the propagation of the electromagnetic field through the partially saturated tuff wall was difficult to interpret under the simplifying assumptions introduced in the model.

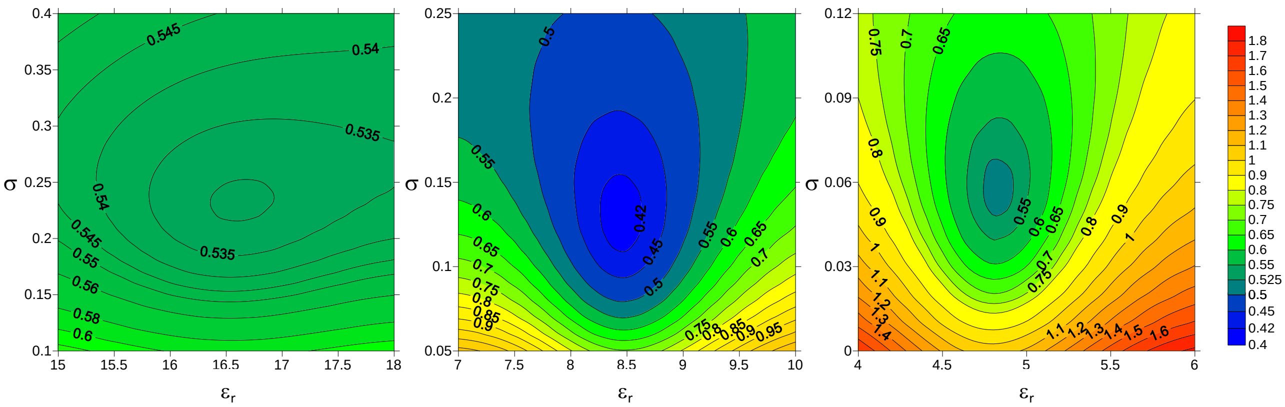

Fig. 6 Contour plots of the objective function ϕ vs. ε_r and σ for three different water contents: maximum saturation (a); end of the drying phase (b); steady conditions (c).

Three examples of the contour plots of the objective function $\varphi(\varepsilon_r,\sigma)$ are shown in Fig. 6 for three different moisture contents of the tuff: maximum degree of saturation, recorded just after the wetting phase (Fig. 6a); end of the drying phase (Fig. 6b); steady conditions recorded at the beginning of the experiment and representing the driest measured condition (Fig. 6c). The corresponding values of the objective function are 0.531, 0.410 and 0.516, respectively. In all cases, and especially for the two driest conditions, a marked minimum of the objective function in the investigated region of the parameter space is clearly visible, indicating a good sensitivity of the GPR response to the variations of dielectric properties related to water content of tuff.

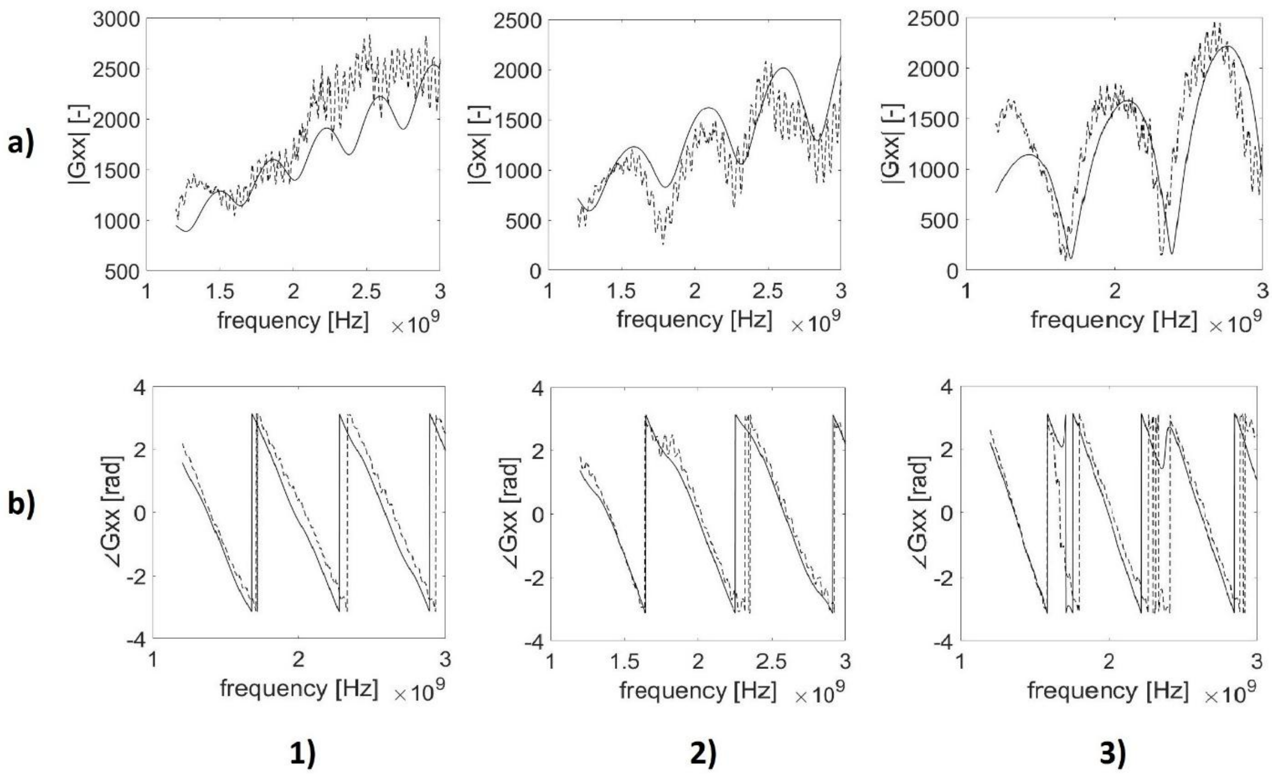

Fig. 7 Amplitude (a) and phase (b) of Green's functions of tuff (with σ constant with frequency) for three different water contents: maximum saturation (1); end of the drying phase (2); steady conditions (3). The dashed and the solid lines represent the observed and the predicted G_{xx}, respectively.

Fig. 7 represents the observed and predicted $\mathrm{G_{xx}}$ in frequency domain for the same three different moisture contents. The phase angle is fairly well described in all the situations, while the amplitude improves with decreasing water content. Two different types of errors may affect the modelling of the amplitude of the Green's function: local disturbance and overall trend. As already stated by Lambot et al. [32], the punctual clutter can be ascribed to the approximation of the metal plate, used for the calibration of the antenna, to an infinite perfect conductor, as well as to the presence of extraneous sources of scattering (e.g. metallic objects) in the laboratory. Conversely, the reason of the general discrepancy between the observed and predicted Green's function amplitudes is harder to identify, as it lies in the hypotheses described in section 2.1 and used to build the model. It is worth noting that also the finite size of the experimental setup and the unrelated scatterers around it may lead to the observed mismatch [32,51].

The plots of the amplitude of $\mathrm{G_{xx}}$ (Fig. 7, a1 to a3) confirm that the effect of the frequency dependence of the electrical conductivity, that should result in a decrease in the amplitude of the Green's function with increasing frequency [40], was not very important in the analysed conditions.

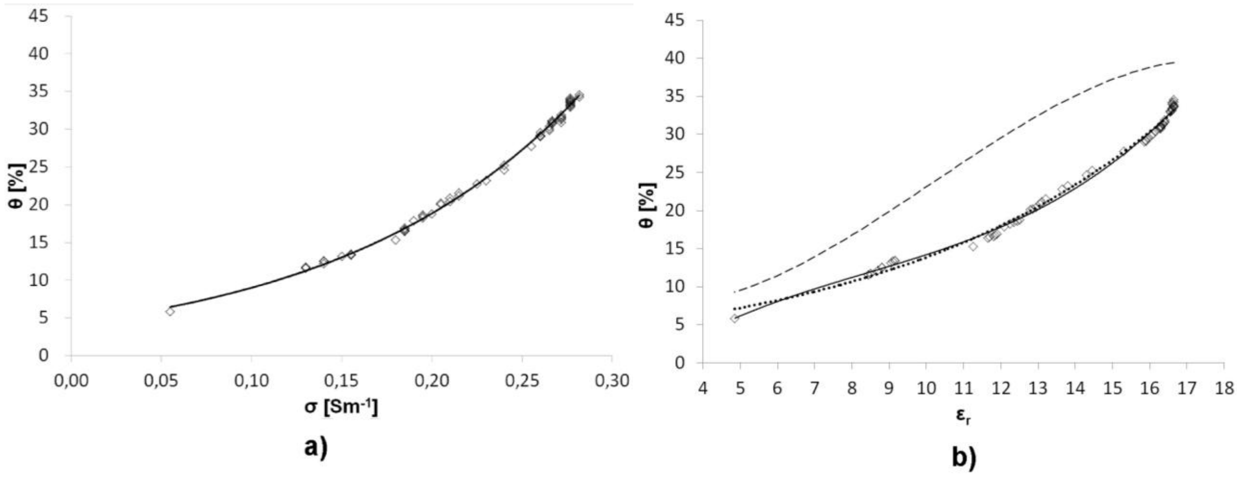

Fig. 8 Experimental points and best-fitting calibration relationships for tuff (eqq. 6, 7 and 8). Panel (a) shows the relationship linking electrical conductivity σ with volumetric water content θ. In panel (b) the identified relationships between relative dielectric permittivity ε_r and θ (solid line for the polynomial and dotted line for the exponential) are compared with the analogous relationship (dashed line) retrieved in our previous research by means of Time Domain Reflectometry [67].

Fig. 8 represents the volumetric water content as a function of the inversely estimated electrical conductivity (Fig. 8a) and relative dielectric permittivity (Fig. 8b).The tuff-specific best-fitting empirical model was retrieved by minimizing the NRMSE of the 64 coupled measurements. The relationship θ(σ) is well described (R^2 = 0.997) by the exponential curve given by:

$$\theta(\sigma) = 4{,}3036e^{7.3891\sigma} \quad (6)$$

The relationship between the dielectric permittivity and the water content, $\theta(\varepsilon_r)$, can be described by an exponential curve (equation 7) and by a third order polynomial (equation 8) similar to Topp's equation for unsaturated soils [67]

$$\theta(\varepsilon_r) = 3.7615e^{0.1305\varepsilon_r} \quad (7)$$

$$\theta(\varepsilon_r) = 0.0169\varepsilon_r^3 - 0.4262\varepsilon_r^2 + 5.0446\varepsilon_r - 10.4974 \quad (8)$$

Although the exponential curve slightly overestimates the water content in dry conditions, the closeness of R^2 to 1 for both the retrieved relationships (R^2 = 0.989 and R^2 = 0.995, respectively), indicates a good fit of the obtained curves to the experimental results over the entire investigated water content range.

The obtained calibration curves show that both electrical conductivity and dielectric permittivity measured by means of GPR are a good proxy for volumetric water content of tuff. However, as the bulk electrical conductivity of tuff depends on the electrical conductivity of pore water, and hence on the dissolved ions concentration, the $\theta(\varepsilon_r)$ relationship appears more suitable for general use in real masonry elements.

Further research is needed to extend the obtained results towards real applications. The capability of GPR to estimate water content in vertical walls, where heterogeneous water content distribution is likely expected, should be tested. A possible solution to overcome this problem could be using a smaller footprint, e.g. achievable with an antenna of smaller dimensions, compatibly with the thickness of the investigated wall.

5. Conclusions

This study investigates the feasibility of using a stepped frequency GPR system to measure the volumetric water content of tuff bricks. The adopted full search of the solution space to model the measured GPR data allows obtaining the best estimate of permittivity and conductivity.

Measurements were carried out on a real scale tuff wall by coupling GPR signal full wave inverse modelling with gravimetric measurements of tuff brick water content, in the range 0.05 to 0.35. Then, specific calibration curves were obtained by linking the retrieved dielectric permittivity and electrical conductivity to the measured water content of tuff.

The dielectric permittivity of tuff is assumed independent of frequency within the interval considered (1.2 GHz to 3 GHz) and the results obtained indicate that the electrical conductivity can be considered independent of frequency as well.

Important errors affect the mathematical reconstruction of the GPR experimental signals. However, in all cases a clear, unique minimum of the objective function can be found in the investigated region of the parameter space investigated. The occurrence of this minimum indicates an unambiguous link between the dielectric permittivity and electrical conductivity of tuff and its water content.

The experimental results lead to a robust identification of clearly defined monotonic relationships for both dielectric permittivity and electrical conductivity. High correlation values indicate that dielectric permittivity and electrical conductivity are potentially good proxies to determine water content of tuff bricks. Because bulk electrical conductivity strongly depends on the electrical conductivity of the pore water, the relationship linking the dielectric permittivity and water content is preferred in real case studies.

GPR represents a promising indirect technique for reliable measurements of water content in tuff walls. Furthermore, because it is completely non-invasive, it may be considered a potentially suitable method for quantitative monitoring of moisture content of masonry elements in heritage buildings.

Further research will focus on the estimation of the water content in a real wall, extending the proposed model to more complex configurations (e.g. in presence of a plaster layer).

Acknowledgments

This research is part of the Ph.D. project "*Non-invasive moisture measurements in porous building materials*" within the Doctoral Course "A.D.I." of Università degli studi della Campania 'L. Vanvitelli', supported by Campania Region through the P.O.R. Campania FSE 2007-2013, D.D. n. 25, 18/02/2014.

We thank dr. Belen Riveiro for assistance with Laser Scan survey, eng. Fred van der Zwan for support and providing materials for the experimental setup, and eng. Sina N. Dezfuli for providing language help and suggestions that improved the manuscript. We also thank the Faculty of Civil Engineering and Geoscience of Technical University of Delft, which hosted all the experiments at Waterlab.

References

1. R. Brown, Geology and the conservation of antique monuments in Turkey. Environ. Geol. Water Sci. 9.2(1987) 71–84.
2. A. Colella, D. Calcaterra, P. Cappelletti, C. Di Benedetto, A. Langella, L. Papa, A. Perrotta, C. Scarpati, M. De Gennaro, Il Tufo Giallo Napoletano, in: M. De Gennaro, D. Calcaterra, A. Langella (Eds.), Le Pietre Storiche della Campania dall'oblio alla riscoperta, Luciano Editore, Napoli, Italy, 2013, pp. 129–154.
3. A.F. Nielsen, Gamma-ray attenuation used for measuring the moisture content and homogeneity of porous concrete. Build. Sci. 7(1972) 257–263.
4. M.K. Kumaran, M.T. Bomberg, A gamma-spectrometer for determination of density distribution and moisture distribution in building materials, National Research Council Canada, Division of Building Research, 1985.
5. A. Marshall, Detecting Moisture in Buildings Using Infrared Thermography, in: Thermal Infrared Sensing Applied to Energy Conservation in Building Envelopes: Thermosense III, International Society for Optics and Photonics, 1981, pp. 111-118.
6. A. Tavukcuoglu, A. Duzgunes, E.N. Caner-Saltık, S. Demirci, Use of IR thermography for the assessment of surface-water drainage problems in a historical building, Agzikarahan (Aksaray), Turkey, NDT&E Int. 38.5 (2005) 402-410.
7. L. Pel, A.A.J. Ketelaars, O.C.G. Adan, A.A. Van Well, Determination of moisture diffusivity in porous media using scanning neutron radiography, Int. J. Heat Mass Transfer, 36.5(1993) 1261–1267. doi:10.1016/S0017-9310(05)80095-X.
8. P. Semerák, R. Černý, A capacitance method for measuring the moisture content of building materials, Stavebnı´obzor 6(1997) 102-103.
9. T. Hauschild, F. Menke, Moisture measurement in masonry walls using a non-invasive reflectometer, Electronics Letters 34.25 (1998): 2413-2414.
10. Z. Suchorab, Laboratory measurements of moisture in a model red-brick wall using the surface TDR probe, Proc., ECOpole 7.1(2013) 171–176.
11. Z. Suchorab, Non-invasive moisture measurement in building materials, Environmental engineering IV, Taylor & Francis Group, London, 2013, pp. 433-439..
12. K.K. Hansen, S.K. Jensen, L. Gerward, K. Singh, Dual-energy X-ray absorptiometry for the simultaneous determination of density and moisture content in porous structural materials, in: 5th symposium on building physics in the Nordic countries, Chalmers tekniska högskola, 1999. pp. 281-288.
13. S. Roels, J. Carmeliet, Analysis of Moisture Flow in Porous Materials using Microfocus X-ray Radiography, Int. J. Heat Mass Transfer 49.25(2006) 4762–4772.

14. P. Berowski, S.F. Filipowicz, J. Sikora, S. Wojtowicz, Dehumidification of the wall process monitoring using 3D EIT system, in: 15th Conference on the Computation of Electromagnetic Fields COMPUMAG, Vol. 2, Shenyang, China, 2005, pp. 166-67.
15. V. Di Tullio, N. Proietti, M. Gobbino, D. Capitani, R. Olmi, S. Priori, C. Riminesi, E. Giani, Non-destructive mapping of dampness and salts in degraded wall paintings in hypogeous buildings: the case of St. Clement at mass fresco in St. Clement Basilica, Rome. Anal. Bioanal. Chem. 369(2010) 1885-1896.
16. G. Gärtner, R. Plagge, H. Sonntag, Determination of moisture content of the outer wall using hf-sensor technology, gg-projekt 2010.
17. G. Stojanovic, M. Radovanovic, M. Malesev, V. Radonjanin, Monitoring of water content in building materials using a wireless passive sensor, Sensors 10(2010) 4270–4280.
18. A. Minardo, E. Catalano, L. Zeni, R. Agliata, R. Greco, L. Mollo, Measurement of moisture content in masonry materials by active distributed optical fiber sensors, in: Photonic Technologies (Fotonica 2016), 18th Italian National Conference on, IET, 2016, pp. 1-3.
19. P. Hoekstra, A. Delaney, Dielectric properties of soils at UHF and microwave frequencies, Journal of Geophysical Research Solid Earth and Planets 79.11(1974) 1699-1708. DOI: 10.1029/JB079i011p01699.
20. E. Slob, M. Sato, G. Olhoeft, Surface and borehole ground penetrating radar developments, Geophysics 75(2010) 75A103-75A120.
21. M.N. Soutsos, J.H. Bungey, S.G. Millard, M.R. Shaw, A. Patterson, Dielectric properties of concrete and their influence on radar testing, NDT&E Int. 34.6(2001) 419-425.
22. H. Jol, Ground penetrating radar: Theory and applications, Elsevier, 2008.
23. D.R. Huston, N.V. Pelczarski, B. Esser, K.R. Maser, Damage detection in roadways with ground penetrating radar, in: Eighth International Conference on Ground Penetrating Radar, International Society for Optics and Photonics, 2000, pp. 91-95.
24. D. Huston, J. Hu, K. Maser, K. Weedon, C. Adam, Ground penetrating radar for concrete bridge health monitoring applications, Nondestructive Evaluation of Bridges and Highways III, International Society for Optics and Photonics, Newport Beach, CA, 1999, pp. 170-180.
25. C.P. Plati, A. Loizos, Estimation of in-situ density and moisture content in HMA pavements based on GPR trace reflection amplitude using different frequencies, J. Appl. Geophys. 97(2013) 3-10.
26. **F.M. Fernandes, A. Fernandes, J. Pais, Assessment of the density and moisture content of asphalt mixtures of road pavements, Construction and Building Materials 154(2017) 1216-1225.**
27. A.K. Benson, Applications of ground penetrating radar in assessing some geological hazards: examples of groundwater contamination, faults, cavities, J. Appl. Geophys. 33(1995) 177 – 193.
28. J.L. Davis, A.P. Annan, Ground-penetrating radar for high resolution mapping of soil and rock stratigraphy, Geophys. Prospect. 37(1989) 531–551.

29. M. Tallini, A. Giamberardino, D. Ranalli, M. Scozzafava, GPR survey for investigation in building foundations, in: Ground Penetrating Radar, 2004. GPR 2004. Proceedings of the Tenth International Conference on, IEEE, 2004, pp. 395-397.
30. S. Malagodi, L. Orlando, S. Piro, E. Rosso, Location of Archaeological Structures Using GPR Method: Three-Dimensional Data Acquisition, Archaeological Prospection 3(1996) 15-23.
31. M.H. Powers, G.R. Olhoeft, Modelling the GPR response of leaking, buried pipes, in: R.S. Bell, M.H. Cramer (Eds.), Symposium on the Application of Geophysics to Engineering and Environmental Problems 1996, Society of Exploration Geophysicists, 1996, pp. 525-534.
32. S. Lambot, E.C. Slob, I. van den Bosch, B. Stockbroeckx, M. Vanclooster, Modelling of ground-penetrating radar for accurate characterization of subsurface electric properties, IEEE Trans. Geosci. Remote Sens. 42.11(2004) pp. 2555–2568.
33. S. Lambot, I. van den Bosch, B. Stockbroeckx, P. Druyts, M. Vanclooster, E.C. Slob, Frequency dependence of the soil electromagnetic properties derived from ground-penetrating radar signal inversion, Subsurface Sens. Technol. Appl. 6(2005) 73–87.
34. J.A. Huisman, C. Sperl, W. Bouten, J.M. Verstraten, Soil water content measurements at different scales: Accuracy of time domain reflectometry and ground-penetrating radar, J. Hydrol. 45(2001) 48–58.
35. S. Lambot, M. Javaux, F. Hupet, M. Vanclooster, A global multilevel coordinate search procedure for estimating the unsaturated soil hydraulic properties, Water Resour. Res. 38.11(2002) 12-24.
36. S. Lambot, J. Rhebergen, I. van den Bosch, E.C. Slob, M. Vanclooster, Measuring the soil water content profile of a sandy soil with off-ground monostatic ground penetrating radar, VZJ 3(2004) 1063-1071.
37. **L. Capozzoli, E. Rizzo, Combined NDT techniques in civil engineering applications: Laboratory and real test, Construction and Building Materials, 154(2017) 1139-1150.**
38. C. Maierhofer, S. Leipold, Radar investigation of masonry structures, NDT&E Int. 34(2001) 139–147.
39. L. Orlando, E.C. Slob, Using multicomponent GPR to monitor cracks in a historical building, Journal of Applied Geophysics 67(2009) 327-334.
40. C. Patriarca, S. Lambot, M.R. Mahmoudzadeh, J. Minet, E.C. Slob, Reconstruction of sub-wavelength fractures and physical properties of masonry media using full-waveform inversion of proximal penetrating radar, J. Appl. Geophys. 74.1(2011) 26–37.
41. G. De **Donno, L. Di Giambattista, L. Orlando, High-resolution investigation of masonry samples through GPR and electrical resistivity tomography, Construction and Building Materials 154(2017) 1234-1249.**
42. L. Binda, C. Colla, M.C. Forde, Identification of moisture capillarity in masonry using digital impulse radar, J Construct. Building. Mater. 8.2(1994) 101–107.
43. L. Binda, G. Lensi, A. Saisi, NDE of masonry structures: use of radar tests for the characterization of stone masonries, NDT&E International, 31.6(1998) 411-419.

44. F. Kurz, H. Sgarz, Measurement of Moisture Content in Building Materials using Radar Technology, in: International Symposium Non-Destructive Testing in Civil Engineering (NDT-CE), Berlin, Germany, 2015.
45. S. Laurens, J.P. Balayssac, J. Rhazi, G. Klysz, G. Arliguie, Nondestructive evaluation of concrete moisture by GPR: Experimental study and direct modeling, Mater. Struct. 38.9(2005) 827–832.
46. A. Kalogeropoulos, J. van der Kruk, J. Hugenschmidt, S. Busch, K. Merz, Chlorides and moisture assessment in concrete by GPR full waveform inversion, Near Surface Geophysics 9.3(2011) 277–285.
47. R. Du Plooy, G. Villain, S.P. Lopes, A. Ihamouten, X. Dérobert, B. Thauvin, Electromagnetic non-destructive evaluation techniques for the monitoring of water and chloride ingress into concrete: a comparative study, Materials and structures 48.1-2(2015) 369-386.
48. S.F. Senin, R. Hamid, Ground penetrating radar wave attenuation models for estimation of moisture and chloride content in concrete slab, Construction and Building Materials 106(2016) 659-669.
49. L. Binda, MD.E.1: determination of moisture distribution and level using radar in masonry built with regular units, Mater. Struct. 38(2005) 283–288.
50. S. Lambot, M. Antoine, M. Vanclooster, E.C. Slob, Effect of soil roughness on the inversion of off-ground monostatic GPR signal for non-invasive quantification of soil properties, Water Resources Research 42.3(2006). DOI: 10.1029/2005WR004416.
51. S. Lambot, E.C. Slob, I. van den Bosch, B. Stockbroeckx, B. Scheers, M. Vanclooster, Estimating soil electric properties from monostatic ground-penetrating radar signal inversion in the frequency domain, Water Resources Res. 40(2004).
52. C.T. Tai, Dyadic Green Function in Electromagnetic Theory, Piscataway, NJ, IEEE Press, 1994.
53. K. Michalski, J. Mosig, Multilayered media Green's functions in integral equation formulations, IEEE Trans. Antennas Propagat. 45.3(1997) 508-519.
54. A.F. Peterson, S.L. Ray, R. Mittra, Computational Methods for Electromagnetics, New York, Oxford Univ. Press, 1998.
55. E.C. Slob, J. Fokkema, Coupling effects of two electric dipoles on an interface, Radio Sci. 37.5(2002).
56. J. Hipp, Soil electromagnetic parameters as functions of frequency, soil density, and soil moisture, Proc. IEEE 62.1(1974) 98-103.
57. M. Hallikainen, F. Ulaby, M. Dobson, M. El-Rayes, L. Wu, Microwave dielectric behaviour of wet soil, part I: Empirical models and experimental observations, IEEE Trans. Geosci. Remote Sens. 1(1985) 25-34.
58. T. Heimovaara, E. de Winter, W. van Loon, D. Esvald, Frequency dependent dielectric permittivity from 0–1 GHz: Time domain reflectometry measurements compared with frequency domain network analyser measurements, Water Resources Res. 32(1996) 3603–3610.
59. L. West, K. Handley, Y. Huang, M. Pokar, Radar frequency dielectric dispersion in sandstone: Implications for determination of moisture and clay content, Water Resources Res. 39.2(2003) 1026.

60. V. Komarov, S. Wang, J. Tang, Permittivity and measurements, Encyclopedia of RF and microwave engineering, 2005.
61. P. Hansen, N. Mladenović, J.A.M. Pérez, Variable neighbourhood search: methods and applications, Annals of Operations Research 175.1(2010) 367-407.
62. L. Papa, I tufi vulcanici nel costruito storico: Vulnerabilità e possibili trattamenti per la conservazione e il restauro, Università degli Studi di Napoli Federico II, Napoli, Italy, 2011 (doctoral thesis).
63. L. Mollo, R. Greco, Moisture measurements in masonry materials by time domain Reflectometry, J. Mater. Civ. Eng. 23.4(2010) 441-444.
64. M. El-Shenawee, E. Miller, Multiple-incidence/multi-frequency for profile reconstruction of random rough surfaces using the three-dimensional electromagnetic fast multipole model, IEEE Trans. Geosci. Remote Sens. 42.11(2004) 2499–2510.
65. A. Chanzy, A. Tarussov, A. Judge, F. Bonn, Soil water content determination using digital ground penetrating radar, Soil Sci. Soc. Am. J. 60(1996) 1318– 1326.
66. L. Boithias, Radio Wave Propagation, McGraw-Hill, New York, 1987.
67. R. Agliata, L. Mollo, R. Greco, Use of TDR to compare rising damp in three tuff walls made with different mortars, J. Mater. Civ. Eng. 29.4(2016) 04016262.
68. G.C. Topp, J. L. Davis, A.P. Annan, Electromagnetic determination of soil water content: Measurements in coaxial transmission lines, Water resources research 16.3(1980) 574-582.